

Symmetry induced phonon renormalization in few layers of 2H-MoTe₂ transistors: Raman and first-principles studies

Subhadip Das¹, Koyendrila Debnath², Biswanath Chakraborty^{1,3}, Anjali Singh⁴,
Shivani Grover², D. V. S. Muthu¹, U. V. Waghmare² and A. K. Sood^{1*}

¹Department of Physics, Indian Institute of Science, Bangalore 560012, India

²Theoretical Sciences Unit, Jawaharlal Nehru Centre for Advanced Scientific Research, Bangalore-560064, India

³Present address: Department of Physics, Indian Institute of Technology Jammu, Jammu-181221, J&K, India

⁴Center for Study of Science, Technology & Policy (CSTEP), Bangalore 560094, India.

Understanding of electron-phonon coupling (EPC) in two dimensional (2D) materials manifesting as phonon renormalization is essential to their possible applications in nanoelectronics. Here we report *in-situ* Raman measurements of electrochemically top-gated 2, 3 and 7 layered 2H-MoTe₂ channel based field-effect transistors (FETs). While the E_{2g}¹ and B_{2g} phonon modes exhibit frequency softening and linewidth broadening with hole doping concentration (p) up to $\sim 2.3 \times 10^{13}/\text{cm}^2$, A_{1g} shows relatively small frequency hardening and linewidth sharpening. The dependence of frequency renormalization of the E_{2g}¹ mode on the number of layers in these 2D crystals confirms that hole doping occurs primarily in the top two layers, in agreement with recent predictions. We present first-principles density functional theory (DFT) analysis of bilayer MoTe₂ that qualitatively captures our observations, and explain that a relatively stronger coupling of holes with E_{2g}¹ or B_{2g} modes as compared with the A_{1g} mode originates from the in-plane orbital character and symmetry of the states at valence band maximum (VBM). The contrast between the manifestation of EPC in monolayer MoS₂ and those observed here in a few-layered MoTe₂ demonstrates the role of the symmetry of phonons and electronic states in determining the EPC in these isostructural systems.

Keywords: Raman spectroscopy, field-effect transistor, electron-phonon coupling, MoTe₂, first-principles density functional theory, hole doping

I. INTRODUCTION

The discovery of unique and remarkable properties of graphene has sparked unprecedented interest in other classes of two dimensional (2D) materials like transition metal dichalcogenides (TMDs, MX₂, where M= transition metals (Mo, W, Ti, Nb, Ta) and X= chalcogens (S, Se, Te)) for their potential applications in nano and optoelectronics [1]. Optical and electrical properties of these TMDs can be easily manipulated by both changing the layer number and carrier doping. MoTe₂ is a member of the group-VI TMD family that crystallizes into three stable phases: Hexagonal (α or 2H) [2], monoclinic (β or 1T') [3] and orthorhombic (γ or T_d) [4]. The 2H phase is semiconducting [5], whereas the 1T' phase is a narrow band gap semiconductor [6]. Similar to other group-VI dichalcogenides, 2H-MoTe₂ has a trigonal-prismatic coordinated crystal structure [7], consisting of weakly coupled sandwich layers of Te-Mo-Te units, where Mo-atom layer is enclosed between two Te layers (Fig. 1(a)) [2]. Unlike other TMDs, energy difference between the 2H and 1T' phase is very small (~ 31 meV per formula unit [8]). This enables easy tuning of the two phases by strain [9, 10], laser irradiation [11, 12] and electron doping [13, 14], making this material an ideal candidate for next generation homojunction devices [15]. From electron doping (n) induced transition from 2H to 1T' phase in multilayer MoTe₂, Zakhidov *et al.* recently suggested that

doped electrons by ionic liquid (IL) gating are localized on the top few layers of the nanocrystal [14], consistent with previous theoretical calculations [16].

Bulk MoTe₂ has an indirect band gap of ~ 1.0 eV [18, 19] which becomes a direct band gap semiconductor in a monolayer with an emission peak of excitonic photoluminescence (PL) spectrum in the near-infrared range (~ 1.1 eV) [5]. This enables the material to be a highly sensitive photodetector [20, 21] and light-emitting diode [22, 23]. With device performance at par with its sister compounds MoS₂ and MoSe₂ [24], MoTe₂ shows ambipolar transport properties [25], which has been recently implemented as a p-n homojunction rectifier device with low charge trapping at the junction interface [26]. Since the exploration of these properties has been mostly carried out in monolayer regime, investigation of the charge localization at high gate bias in few layers of the nanocrystal can open up new possibilities in the field of opto-electronics.

Carrier concentration in a semiconductor can be modulated by injecting resonant photons from light emitting diode [27–29], substitutional doping during growth process [30] and application of an electrostatic field on the channel of a FET [31–34]. Electrolyte gating has gained immense interest recently for electrostatic modulation of carrier density up to $\sim 10^{15}/\text{cm}^2$ [35] owing to their large dielectric capacitance. On application of gate voltage, ions move inside the electrolyte to screen the applied electric field to form few Angstroms [36] thick double layers of ions near the device and gate electrode [37, 38]. However electrolyte gating is well known source of electrostatic disorders [39, 40] and is best suited for disorder

* asood@iisc.ac.in

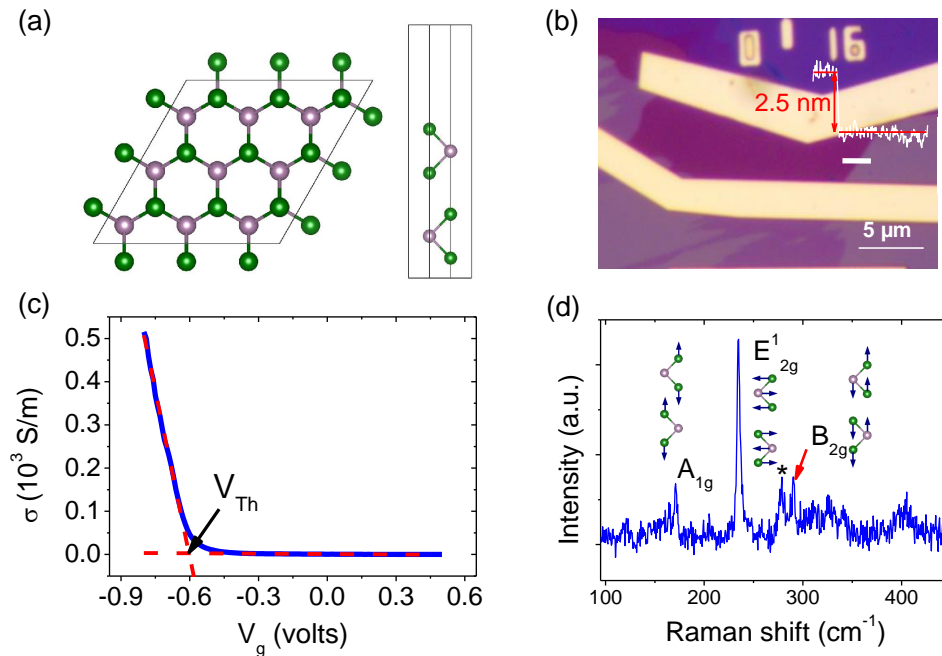


FIG. 1. (a) Top and side view of the crystal structure of bilayer 2H-MoTe₂. Violet and green spheres denote Mo and Te atoms respectively. (b) Optical image of the field-effect transistor (FET) device. Inset image shows the AFM height profile of the nanocrystal. (c) Transfer characteristics of the trilayer FET device. Red dashed lines show the linear fit to the transistor off and on state. The intersection of these lines indicate the current threshold voltage (V_{Th}). (d) Raman spectrum of the trilayer nanocrystal. The star symbol indicates Raman peak from the ionic liquid. Atomic displacements of the phonon modes [17] are indicated in the figure.

robust systems such as superconductors [41, 42].

As Raman spectroscopy does not require any sample preparation, it has been extensively used as a non-invasive, contact-less, fast and accurate tool to determine strain [43], doping effects [13], layer number [17, 44], crystal orientation [45], structural transitions between different polytypes [9, 11–14, 46–48] in few-layer MoTe₂ devices in ambient as well as different sample environments. Furthermore, Raman scattering has been employed in various 2D materials to measure electron-phonon coupling (EPC) that governs electronic transport properties [31, 32]. For n-type semiconducting MoS₂, symmetry of the conduction band minimum (CBM) determines EPC of the A_{1g} and E_{2g}^1 modes [33]. In ambipolar phosphorene transistor, electrons and holes couple differently to phonons as CBM and valence band maximum (VBM) possess different orbital symmetries [34]. Although the electronic band structure of monolayer MoTe₂ is similar to MoS₂ [16], the VBM of the former remains at the K-point from single to three layers [16, 49]. Thus a study of the EPC in few layer MoTe₂, an intrinsic p-type semiconductor [50, 51], will reveal asymmetry of phonon coupling with holes and electrons in these hexagonal polytypes of TMDs.

Bulk MoTe₂ belongs to D_{6h} point-group [52] having six Raman active modes ($A_{1g} + 2B_{2g} + E_{1g} + 2E_{2g}$) [17]. A_{1g} and E_{2g} modes have vibrations perpendicular to and along the basal plane of the lattice, respectively [17]. The

in-plane E_{1g} mode is absent in backscattering configuration [17]. Notably, the translation symmetry along the z -direction is broken in a few layer nanocrystal, reducing the symmetry to D_{3h} and D_{3d} for odd and even layers of MoTe₂, respectively [52]. Thus, the out-of-plane inactive mode B_{2g} in bulk becomes Raman active in few layers and shows highest intensity in a bilayer nanocrystal [53]. For odd layer nanocrystal, the inversion symmetry breaks, making some modes both Raman and infrared active [17]. For simplicity, the Raman modes of even and odd layers of MoTe₂ in this paper are represented by the bulk phonon symmetry group of equivalent atomic displacements (see table-S1 of the supplemental material (SM)).

In the present study, we measure in-operando optical phonons in a few layers of 2H-MoTe₂ based field-effect transistors (FETs) as a function of hole doping concentration (p) up to $\sim 2.3 \times 10^{13} \text{ cm}^{-2}$. The modes involving both metal and chalcogen atom vibrations, E_{2g}^1 and B_{2g} [17] show phonon softening and linewidth broadening while the A_{1g} mode with out-of-plane vibrations of only the chalcogen atoms [17], shows in contrast, relatively smaller phonon hardening and linewidth sharpening. The frequency renormalization comparison of E_{2g}^1 mode from 2, 3 and 7 layer devices indicate that the doping is confined to only two top layers of the nanocrystal. We have carried out first-principles density functional theory (DFT) calculations on a bilayer MoTe₂ transis-

tor for understanding the experimental results. We show that the holes couple weakly with the A_{1g} mode as compared to E_{2g}^1 and B_{2g} modes and demonstrate that different orbital symmetries of the VBM and CBM at the K-point of MoTe_2 and MoS_2 , respectively, contribute to their contrasting EPC.

II. RESULTS AND DISCUSSION

A. Experimental results

Bulk MoTe_2 crystals were mechanically exfoliated and transferred to a clean Si/SiO_2 (285 nm) substrate. Device contacts were fabricated by first patterning them in electron-beam lithography followed by thermal evaporation of 5 and 50 nm thick chromium and gold respectively. The optical image of the two-probe device is shown in Fig. 1(b). Atomic force microscope (AFM) measurement in tapping mode (inset graph of Fig. 1(b)) confirms the nanocrystal thickness to be ~ 2.5 nm (~ 3 monolayers). A drop of 1-ethyl-3-methylimidazolium bis(trifluoromethylsulfonyl)imide (EMIM-TFSI) IL was drop casted on top of the device channel for electrochemical top gating. Electrical measurements were done using a Keithley 2400 source meters. Conductivity (σ) as a function of gate voltage (V_g) shows hole transport (Fig. 1(c)) due to unintentional doping from the environment. Previous experiments done on few layer MoTe_2 show formation of Mo-O bonds on tellurium vacancy sites which shift the Fermi level towards the VBM, making MoTe_2 intrinsically hole doped [50, 51]. To determine hole doping, p , from V_g , we use parallel plate capacitor formula, $p = C_G(V_g - V_{Th})$, where V_{Th} is the current threshold voltage, and the gate capacitance of the IL, C_G is taken to be $\sim 5.9 \mu\text{F}/\text{cm}^2$ [54]. Consistent with previous reports [55, 56], the device shows field-effect mobility $\sim 1.85 \text{ cm}^2/\text{V}\cdot\text{s}$ and current on/off ratio $\sim 10^5$.

In-situ transport and Raman measurements in backscattering configuration were done at room temperature using LabRAM HR-800 Evolution spectrometer having 1800 lines/mm gratings and a Peltier cooled CCD detector. Excitation laser of 532 nm wavelength was focused using a $50\times$ long working distance objective with incident power less than 0.5 mW to avoid heating. Raman spectrum of the trilayer nanocrystal is shown in Fig. 1(d). At each gate voltage, the peaks are fitted with a sum of Lorentzian functions to extract the phonon frequency (ω) and linewidth (γ). Figs. 2(a) and (b) show the change in phonon frequency from zero doped state ($\Delta\omega = \omega_{n\neq 0} - \omega_{n=0}$) and linewidth of the trilayer nanocrystal, respectively, with hole doping concentration up to $\sim 1.1 \times 10^{13}/\text{cm}^2$. The frequency of the in-plane mode E_{2g}^1 decreases and linewidth broadens whereas the out-of-plane mode, A_{1g} shows in contrast, relatively small phonon hardening and linewidth sharpening. We have repeated our experiments for a bilayer nanocrystal. We have used a FET device with both bi-

layer and multilayer channels in parallel to confirm our doping effect in the electrical transfer characteristic (see Fig. S1(a) of the SM). Electrochemical gating induced ions sit very close (\sim few Angstrom [36]) to the semiconductor surface in a FET. Using EMIM-TFSI gating on a hexagonal boron-nitride enclosed strontium titanate (STO), a two-dimensional electron gas system (2DES), Gallagher *et al.* [40] have shown that disorders induced by the IL reduces the mobility by an order of magnitude. Xia *et al.* [39] theoretically explained this effect in terms of 2D percolative transport from trapped carriers due to the ions induced by the IL at the semiconductor-electrolyte interface. Hence, the mobility suppression will be higher in monolayer and bilayer channels resulting in negligible transistor performance.

As the intensity of the A_{1g} Raman mode is weak for 532 nm laser excitation for few layers of MoTe_2 [5], we have used excitation wavelength of 660 nm (Fig. S1(b) of the SM) for this device. With hole doping concentration up to $\sim 1.5 \times 10^{13}/\text{cm}^2$, similar to the trilayer nanocrystal (Figs. 2(a) and (b)), A_{1g} mode shows a trend of phonon hardening and linewidth sharpening to a small extent and the E_{2g}^1 mode shows phonon softening and linewidth broadening (Figs. 2(c) and (d)). The nature of the A_{1g} mode as reported by Grzeszczyk *et al.* [44], depends on the thickness of the MoTe_2 nanocrystal. They have shown that at 633 nm of laser excitation, A_{1g} is a single peak both in monolayer and bilayer nanocrystals [44]. However, the intensity of the peak drops below E_{2g}^1 and splits into multiple peaks in multilayer nanocrystals of 2H- MoTe_2 [44]. The single peak of the A_{1g} mode in the observed Raman spectrum at 660nm of laser excitation shown in Fig. S1(b) combined with AFM data in Fig. S1(a), confirm that the doping dependence presented in Figs. 2(c) and (d) are indeed from the bilayer part of the device (Fig. S1(a)). In addition, the observed trend of $\Delta\omega$ and γ is similar to the isolated trilayer nanocrystal (Figs. 2(a) and (b)), confirming the effect of hole doping. However, the transfer characteristics shown in Fig. S1(a) is dominated by the multilayer nanocrystal. Furthermore, the threshold voltage for Raman frequency and linewidth shift of the bilayer nanocrystal (Figs. 2(c) and (d)) matches well with the threshold voltage in the transfer characteristics (Fig. S1(a)). It is to be noted that for similar reasons, parallel channels of bulk and monolayer of black phosphorus nanocrystal were used to determine phonon renormalisation with doping [34].

As the frequency of the Raman mode from the IL (see Fig. S2 of the SM) is close to the B_{2g} mode at $\sim 290 \text{ cm}^{-1}$ (Fig. 1(d)), we did experiments on a seven-layer thick nanocrystal, where the Raman signal (with 532 nm wavelength of laser excitation) is more prominent (Fig. 3(a)). Fig. 3(b) shows the thickness of the nanocrystal to be ~ 5 nm (\sim seven layers) from AFM measurement (inset graph of Fig. 3(b)). The device transfer characteristics in Fig. 3(b) shows hole field-effect mobility of $\sim 0.41 \text{ cm}^2/\text{V}\cdot\text{s}$ and current on/off ratio $\sim 10^2$. Using SiO_2 back gate, Pradhan *et al.* [24], showed similar transis-

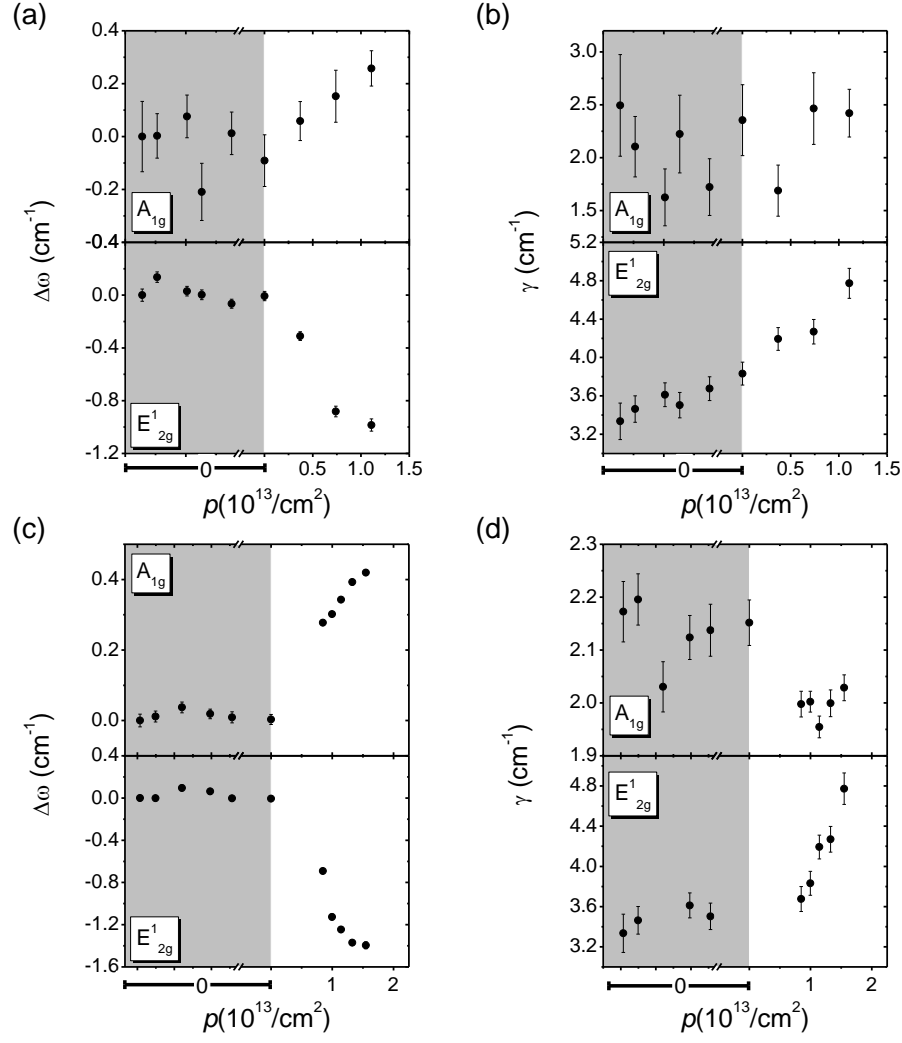


FIG. 2. Change in the frequency ($\Delta\omega=\omega_{n\neq 0}-\omega_{n=0}$) and linewidth (γ) of the Raman modes with hole doping concentration (p) for (a and b) trilayer and (c and d) bilayer nanocrystal, respectively. Gray regions represent the zero doped state ($V_g \leq V_{Th}$). Change in the horizontal axis increments below zero doping is represented by the break symbol.

tor characteristic of trilayer and seven-layer nanocrystals, since few-layer MoTe_2 is an indirect bandgap semiconductor with small change in bandgap from monolayer to bulk [5]. At ambient condition, the seven-layer nanocrystal is initially unintentionally hole doped (Fig. 3(b)) as compared to the trilayer nanocrystal (Fig. 1(c)). Thus the dielectric screening of the gate voltage can account for the relatively smaller mobility and current on-off ratio in seven layer crystal as compared with the trilayer nanocrystal. With hole doping up to $\sim 2.3 \times 10^{13}/\text{cm}^2$, the in-plane vibrational mode, E_{2g}^1 shows phonon softening and linewidth broadening (Figs. 3(c) and (d)), similar to trilayer and bilayer nanocrystal (Fig. 2). The B_{2g} mode, although having similar vibrational displacements to the A_{1g} mode [17], shows phonon renormalization as the in-plane E_{2g}^1 mode.

Brumme *et al.* [16] theoretically showed that the charges localize only in the topmost two layers due to

screening effects in MoTe_2 based FET devices. From electron doping induced 2H to 1T' phase transition from bulk to monolayer MoTe_2 , Zakhidov *et al.* experimentally showed that the gating by IL causes electrons to be confined in the topmost few layers [14]. Consistent with these reports, we observe a smaller change in $\Delta\omega$ and γ of E_{2g}^1 mode for a given gate voltage as the layer number increases (Figs. 2, 3(c) and 3(d)). Taking the applied doping (p) to be limited to the top two layers rather than the entire nanocrystal, the average doping (p') for a N -layer nanocrystal is scaled as $p' = p \times 2/N$. With p' , $\Delta\omega$ of E_{2g}^1 from 2, 3 and 7 layer nanocrystal scale very well with each other (Fig. 4(a)), justifying that the doping is confined to top two layers of the nanocrystal. The scaling of γ for the three devices (Fig. 4(b)) is modest with p' .

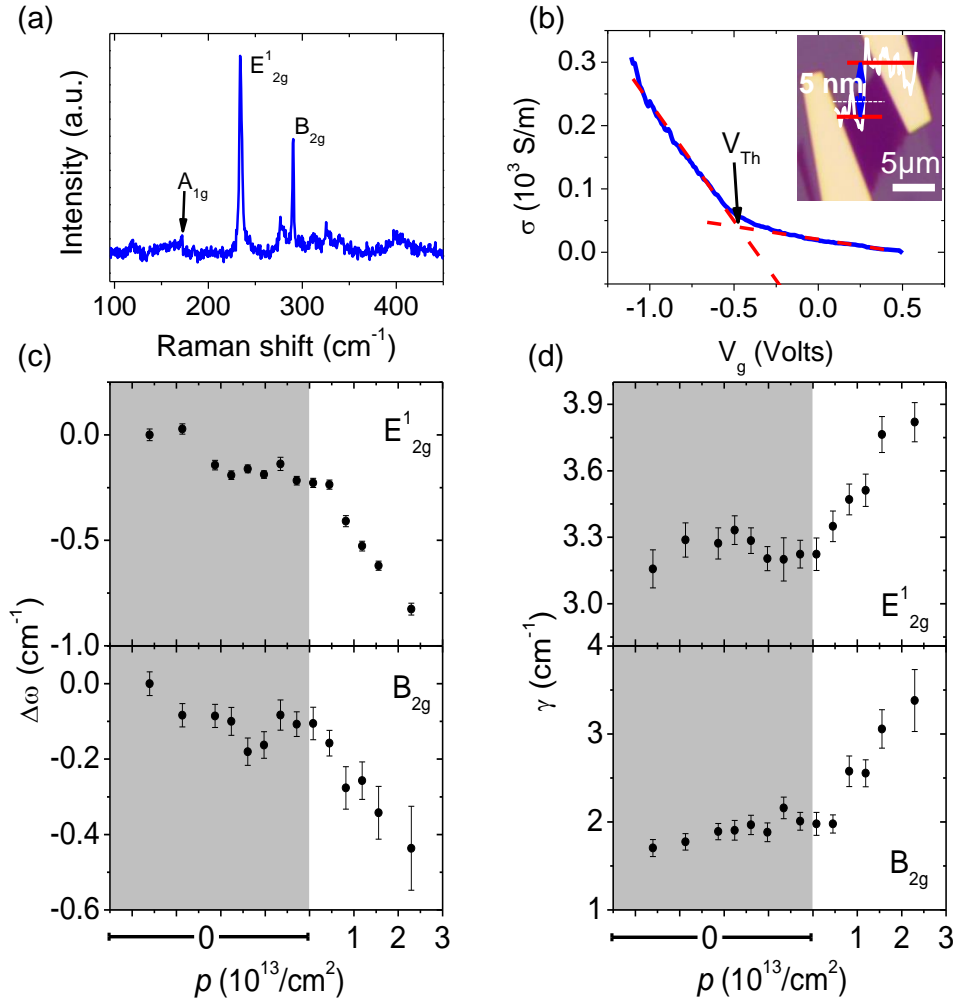


FIG. 3. (a) Raman spectrum of the seven-layer nanocrystal. (b) Transfer characteristics of the FET device. Similar to the fit on Fig. 1(c), V_{Th} is indicated in the figure. Inset graph shows the AFM height profile of the nanocrystal. (c) $\Delta\omega$ and (d) γ versus p of E_{2g}^1 and B_{2g} modes.

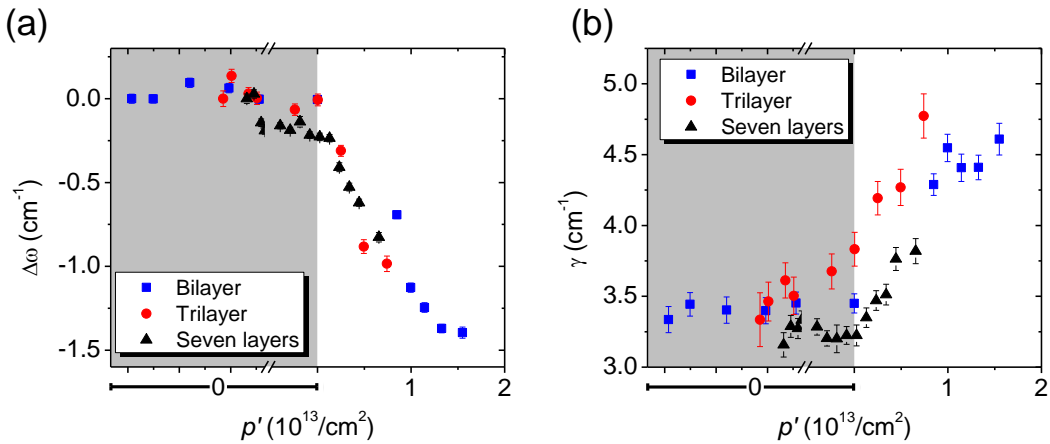


FIG. 4. (a) $\Delta\omega$ and (b) γ with average doping concentration (p') of the E_{2g}^1 mode in 2, 3 and 7 layer nanocrystal.

B. Theoretical analysis

Our first-principles DFT calculations of the bilayer were carried out with Quantum ESPRESSO (QE) pack-

age [57], in which we treat only the valence electrons by effectively replacing the potential of ionic cores with

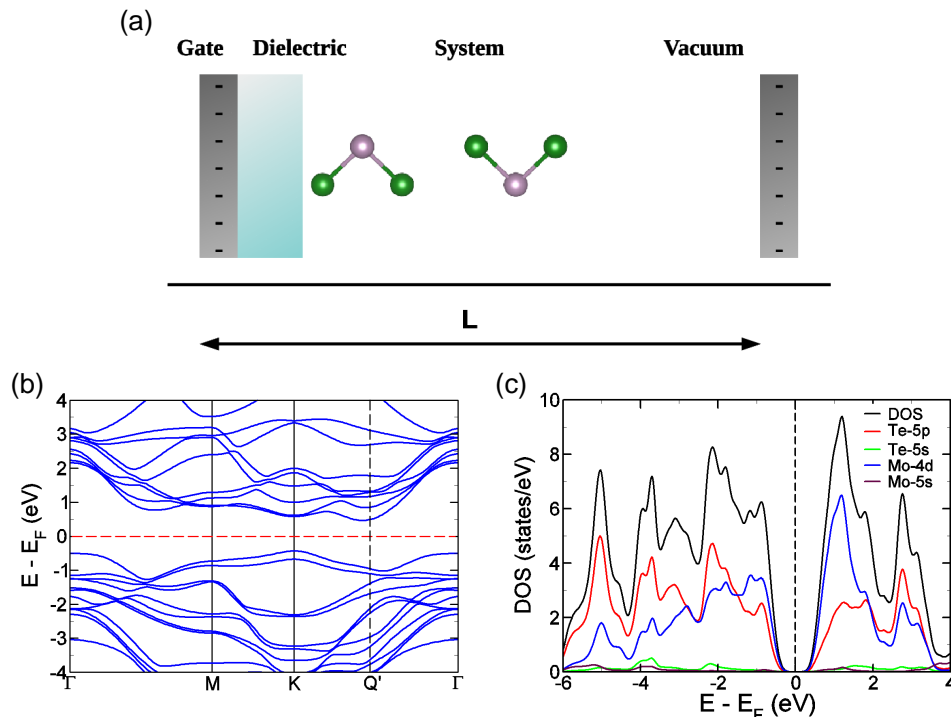


FIG. 5. (a) Schematic illustration of an FET setup simulated in a periodically repeated unit cell where the layers of 2H-MoTe₂ is placed in front of a charged plane mimicking the metallic gate (shown with gray color plate). The layers are doped with holes, such that the charged plane is charged with the same magnitude of opposite charges. To mimic the dielectric separation layer, we include a potential barrier (shown in blue). The length of the unit cell along the z -direction is given by L . (b) Electronic structure of bilayer 2H-MoTe₂ calculated including the effect of spin-orbit coupling, shows it to be an indirect band gap semiconductor with VBM at K and CBM at Q' point (Q' point is along Γ -K direction) with a band gap of 0.88 eV. (c) Projected density of states of bilayer 2H-MoTe₂ shows a strong coupling between the Mo d orbitals and Te p orbitals evident in their joint contributions to states near the gap.

pseudopotentials. Exchange-correlation energy of electrons is included within a generalized gradient approximation (GGA) [58] in the functional form parametrized by Perdew, Burke, and Ernzerhof [59]. We include spin-orbit coupling (SOC) through use of relativistic pseudopotentials and a second variational procedure [60]. Kohn-Sham wave functions and charge density were represented in plane wave basis sets truncated at energy cut-offs of 40 Ry and 320 Ry respectively. A vacuum layer of 10 Å has been introduced parallel to MoTe₂ layer (perpendicular to z -direction) to weaken the interaction between the layer and its periodic images. Brillouin zone (BZ) integrations were sampled on uniform $24 \times 24 \times 1$ mesh of \mathbf{k} -points. The discontinuity in occupation numbers of electronic states was smeared using a Fermi-Dirac distribution function with broadening temperature of $k_B T = 0.003$ Ry. We include van der Waals (vdW) interaction using PBE + D2 parametrized scheme of Grimme [61].

We have used the FET setup [62] as implemented in QE package to treat gating electric field. A 2D charged plate modeling the gate electrode is placed at $z = 0.019 L$. A potential barrier with a height of $V_0 = 0.09$ Ry and a width of $d_b = 0.1 L$ is used to model the dielectric

layer, preventing ions from moving too close to the gate electrode (Fig. 5(a)). Dynamical matrices were calculated within the Density Functional Perturbation Theory (DFPT) [63] on a $3 \times 3 \times 1$ mesh of q -vectors in the Brillouin zone. Fourier interpolation of these dynamical matrices was done to obtain phonon frequencies at arbitrary wavevectors and dispersion along the high symmetry lines in the Brillouin zone.

Bilayer 2H-MoTe₂ has a hexagonal structure, where covalently bonded layers of Te-Mo-Te atomic planes are stacked along c -axis interacting via weak vdW interaction. The periodic unit cell of bilayer 2H-MoTe₂ is characterized by a stacking sequence $AbABaB$, where Wyckoff positions A, B label basal Te atomic planes and a, b label Mo atomic planes of the hexagonal lattice (Fig. 1(a)). Our estimate of the lattice parameter a ($= b$) is 3.53 Å which matches well with previous experimental value [64]. Bilayer 2H-MoTe₂ is an indirect band gap semiconductor with VBM at K and CBM at Q' point (along Γ -K direction) separated by a gap of 0.88 eV (Fig. 5(b)). From the projected electronic density of states (DOS) (calculated without SOC) (Fig. 5(c)), it is evident that there is a rather strong coupling between the Mo d orbitals and Te p orbitals, contributing to states near the

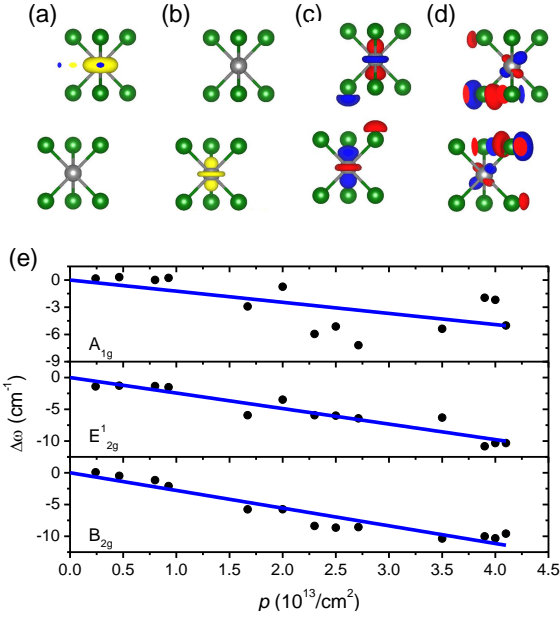


FIG. 6. Isosurfaces of wavefunctions of states at (a) VBM and (b) CBM at K-point showing in-plane d_{xy} and out-of-plane d_{z^2} orbital (Mo) character respectively. Isosurfaces of wavefunctions of states at (c) VBM and (d) CBM at Γ -point. Clearly, VBM at Γ -point is formed of out-of-plane (Mo d_{z^2} and Te p_z) orbitals and CBM has contributions mainly from out-of-plane Mo and in-plane Te states (Mo d_{z^2} and Te $p_{x/y}$). (e) Changes in frequencies of A_{1g} , E_{2g}^1 and B_{2g} modes as a function of hole concentration p . E_{2g}^1 and B_{2g} modes soften more significantly with hole doping than the A_{1g} mode. Blue lines represent linear fit to the data with slope of -1.23 , -2.44 and $-2.78 \text{ cm}^{-1}/(10^{13} \text{ cm}^{-2})$ for A_{1g} , E_{2g}^1 and B_{2g} modes, respectively.

$$\lambda_{q\nu} = \frac{2}{\hbar\omega_{q\nu}N(\epsilon_f)} \sum_k \sum_{mn} |g_{k+q, k}^{q\nu, ij}|^2 \times \delta(\epsilon_{k+q, i} - \epsilon_f) \times \delta(\epsilon_{k, j} - \epsilon_f), \quad (1)$$

where ω and $N(\epsilon_f)$ are the phonon frequency and electronic density of states at the Fermi energy, respectively. The EPC matrix element is given by

$$g_{k+q, k}^{q\nu, ij} = \left(\frac{\hbar}{2M\omega_{q\nu}}\right)^{\frac{1}{2}} \langle \psi_{k+q, i} | \Delta V_{q\nu} | \psi_{k, j} \rangle, \quad (2)$$

where $\psi_{k, j}$ is the electronic wave function with wave vector \mathbf{k} and energy eigenvalue $\epsilon_{k, j}$ for band j , and M is the ionic mass. $\Delta V_{q\nu}$ is the change in the self-consistent potential induced by atomic displacements of phonon $\mathbf{q}\nu$. The calculated values of EPC of B_{2g} and A_{1g} modes are 0.016 and 0.011 respectively, consistent with the experimental observation that B_{2g} phonon is renormalized more with the hole doping.

It is interesting to compare these trends with the phonon renormalization seen in n-doped monolayer MoS₂

gap. Visualization of wavefunctions of states at VBM and CBM at Γ and K-points confirms the contribution of specific d-orbitals of Mo and p-orbitals of Te (Fig. 6(a-d)). The doped holes occupy the states at the K-point. With increasing hole-doping, holes continue to accumulate in states at K-point because energy separation between valence band of Q' valley and valence band states at K-point is rather large ($\sim 490 \text{ meV}$) (Fig. 5(b)). We find that inclusion of SOC in our calculations leads to notable reduction in the indirect band gap by 60 meV and hence we have included SOC in further calculations.

We simulated hole doping in 2H-MoTe₂ bilayer by adding a small fraction of holes (close to the experimental doping concentration) to its unit cell. From the changes in calculated frequencies with their linear fits (Fig. 6(e)), it can be seen that $\Delta\omega$ for A_{1g} mode is $\sim -5.1 \text{ cm}^{-1}$ for $p = 4.1 \times 10^{13}/\text{cm}^2$, in contrast to corresponding higher softening of E_{2g}^1 mode by 10.2 cm^{-1} and B_{2g} mode by 11.4 cm^{-1} . The magnitude of the slope $S (= |d(\Delta\omega)/dp|)$ for the A_{1g} mode is least, indicating smallest change of this mode frequency (compared to E_{2g}^1 and B_{2g}) with doping. Although DFT analysis qualitatively captures the experimental trend of $\Delta\omega$ versus p for E_{2g}^1 and B_{2g} (Figs. 2, 3(c) and 3(d)), the relatively smaller phonon hardening observed in experiments for the A_{1g} mode (as compared to E_{2g}^1 and B_{2g} modes) is not captured in our DFT analysis.

In order to understand why A_{1g} and B_{2g} are affected differently, we have calculated the EPC of pristine bilayer without inclusion of SOC to understand these trends, as estimation of EPC with doping in FET geometry is not currently implemented in the QE code. The EPC of a mode ν at momentum \mathbf{q} (with frequency $\omega_{q\nu}$) is calculated as [33]

[33]. Electron doping in monolayer MoS₂ has contrasting effects on the frequencies of A_{1g} and E_{2g}^1 optic modes [33]. While A_{1g} mode softens significantly ($\sim 7 \text{ cm}^{-1}$ at $\sim 1.8 \times 10^{13}/\text{cm}^2$), E_{2g}^1 remains unaffected [33]. We can understand this contrast as follows: monolayer MoS₂ is a direct band-gap semiconductor with a gap of $\sim 1.8 \text{ eV}$ with the VBM and CBM at the K-point [49]. The CBM at the K-point of MoS₂ has contribution from the out-of-plane d_{z^2} orbital of Mo atoms [33]. The A_{1g} mode has the symmetry of the lattice, hence matrix element $\langle \psi_{k+q, i} | \Delta V_{q\nu} | \psi_{k, j} \rangle$ is non zero [33]. In contrast, matrix element $\langle \psi_{k+q, i} | \Delta V_{q\nu} | \psi_{k, j} \rangle$ of in-plane vibrational mode E_{2g}^1 vanishes as it is orthogonal to A_{1g} irreducible representation [33]. In comparison, hole doping in bilayer 2H-MoTe₂ leads to occupation of states at the top of the valence band at the K-point, having domi-

nance of in-plane d_{xy} orbitals (odd symmetry states) of Mo. The crystal symmetry at K-point is point group C_2 which is a nontrivial subgroup of D_{3d} and the symmetry of the valence band is A_{2u} . The matrix element $\langle \psi_f | \Delta V_{q\nu} | \psi_i \rangle$ (where i and f are the initial and final electronic wavefunctions) for $\nu = A_{1g}$, E_{2g}^1 and B_{2g} modes are non-zero as calculated using direct product table for C_2 . Hence, changes in occupancy of these states as a function of doping result in renormalization of these modes. Though A_{1g} and B_{2g} modes have different symmetries in bulk, the modes reduce to the same symmetry, A_{1g} in the case of bilayer (symmetry in even layer, odd layer, and bulk MoTe_2 has been listed in table S1), softening is stronger for B_{2g} mode as compared to A_{1g} . This is consistent with the EPC being slightly higher for the B_{2g} (0.016) than the A_{1g} (0.011) mode and is also evident in frequency versus hole doping concentration plot (Fig.6(e)).

III. CONCLUSIONS

In FET devices with 2, 3 and 7 layers of MoTe_2 as channels, we have demonstrated that hole doping induces phonon softening and linewidth broadening of the E_{2g}^1 and B_{2g} modes, while the A_{1g} mode shows relatively small phonon hardening and linewidth sharpening. Due to dielectric screening, we find that holes are induced

only in the top two layers of these channels upon electrochemical top gating, as evident in the layer dependent frequency softening of the E_{2g}^1 mode. Results of our first-principles density functional theory calculations agree qualitatively with our experiments. Interestingly, effects of EPC in hole doped MoTe_2 observed here are in sharp contrast to the trends seen earlier in electron doped monolayer MoS_2 . We explain this in terms of the difference in symmetry of their frontier states relevant to electron and hole doping. In addition to being relevant to use Raman spectroscopy as a non-invasive tool for characterization of MoTe_2 -FET devices, our study will be useful in understanding the role of relevant phonon interaction with charge carriers in determining carrier mobility in MoTe_2 devices.

ACKNOWLEDGMENT

We thank the Centre for Nanoscience and Engineering department (CeNSE) of IISc for device fabrication facilities. AS is thankful to JNCASR for postdoctoral fellowship. AKS thanks Department of Science and Technology (DST), India for support under the Nanomission project and Year of Science Professorship. UVW acknowledges support from a J. C. Bose National Fellowship of SERB-DST, Govt. of India and an AOARD project from United States Air Force.

-
- [1] Q. H. Wang, K. Kalantar-Zadeh, A. Kis, J. N. Coleman, and M. S. Strano, *Nature nanotechnology* **7**, 699 (2012).
 - [2] D. Puotinen and R. E. Newham, *Acta Crystallographica* **14**, 691 (1961).
 - [3] B. E. Brown, *Acta Crystallographica* **20**, 268 (1966).
 - [4] Y. Qi, P. G. Naumov, M. N. Ali, C. R. Rajamathi, W. Schnelle, O. Barkalov, M. Hanfland, S.-C. Wu, C. Shekhar, Y. Sun, *et al.*, *Nature communications* **7**, 1 (2016).
 - [5] C. Ruppert, O. B. Aslan, and T. F. Heinz, *Nano Letters* **14**, 6231 (2014).
 - [6] D. H. Keum, S. Cho, J. H. Kim, D.-H. Choe, H.-J. Sung, M. Kan, H. Kang, J.-Y. Hwang, S. W. Kim, H. Yang, *et al.*, *Nature Physics* **11**, 482 (2015).
 - [7] J. L. Verble and T. J. Wieting, *Phys. Rev. Lett.* **25**, 362 (1970).
 - [8] Y. Li, K.-A. N. Duerloo, K. Wauson, and E. J. Reed, *Nature communications* **7**, 1 (2016).
 - [9] S. Song, D. H. Keum, S. Cho, D. Perello, Y. Kim, and Y. H. Lee, *Nano Letters* **16**, 188 (2016).
 - [10] W. Hou, A. Azizimanesh, A. Sewaket, T. Peña, C. Watson, M. Liu, H. Askari, and S. M. Wu, *Nature nanotechnology* **14**, 668 (2019).
 - [11] S. Cho, S. Kim, J. H. Kim, J. Zhao, J. Seok, D. H. Keum, J. Baik, D.-H. Choe, K. J. Chang, K. Suenaga, S. W. Kim, Y. H. Lee, and H. Yang, *Science* **349**, 625 (2015).
 - [12] Y. Tan, F. Luo, M. Zhu, X. Xu, Y. Ye, B. Li, G. Wang, W. Luo, X. Zheng, N. Wu, Y. Yu, S. Qin, and X.-A. Zhang, *Nanoscale* **10**, 19964 (2018).
 - [13] Y. Wang, J. Xiao, H. Zhu, Y. Li, Y. Alsaied, K. Y. Fong, Y. Zhou, S. Wang, W. Shi, Y. Wang, *et al.*, *Nature* **550**, 487 (2017).
 - [14] D. Zakhidov, D. A. Rehn, E. J. Reed, and A. Salleo, *ACS Nano* **14**, 2894 (2020).
 - [15] R. Ma, H. Zhang, Y. Yoo, Z. P. Degregorio, L. Jin, P. Golani, J. Ghasemi Azadani, T. Low, J. E. Johns, L. A. Bendersky, A. V. Davydov, and S. J. Koester, *ACS Nano* **13**, 8035 (2019).
 - [16] T. Brumme, M. Calandra, and F. Mauri, *Phys. Rev. B* **91**, 155436 (2015).
 - [17] G. Froehlicher, E. Lorchat, F. Fernique, C. Joshi, A. Molina-Sánchez, L. Wirtz, and S. Berciaud, *Nano Letters* **15**, 6481 (2015).
 - [18] A. Conan, D. Delaunay, A. Bonnet, A. G. Moustafa, and M. Spiesser, *physica status solidi (b)* **94**, 279 (1979).
 - [19] A. J. Grant, T. M. Griffiths, G. D. Pitt, and A. D. Yoffe, *Journal of Physics C: Solid State Physics* **8**, L17 (1975).
 - [20] K. Zhang, X. Fang, Y. Wang, Y. Wan, Q. Song, W. Zhai, Y. Li, G. Ran, Y. Ye, and L. Dai, *ACS Applied Materials & Interfaces* **9**, 5392 (2017).
 - [21] M. Kuri, B. Chakraborty, A. Paul, S. Das, A. K. Sood, and A. Das, *Applied Physics Letters* **108**, 063506 (2016).
 - [22] Y. Li, J. Zhang, D. Huang, H. Sun, F. Fan, J. Feng, Z. Wang, and C.-Z. Ning, *Nature nanotechnology* **12**, 987 (2017).
 - [23] Y.-Q. Bie, G. Grosso, M. Heuck, M. M. Furchi, Y. Cao, J. Zheng, D. Bunandar, E. Navarro-Moratalla, L. Zhou, D. K. Efetov, *et al.*, *Nature nanotechnology* **12**, 1124

- (2017).
- [24] N. R. Pradhan, D. Rhodes, S. Feng, Y. Xin, S. Memaran, B.-H. Moon, H. Terrones, M. Terrones, and L. Balicas, *ACS Nano* **8**, 5911 (2014).
- [25] S. Nakaharai, M. Yamamoto, K. Ueno, Y.-F. Lin, S.-L. Li, and K. Tsukagoshi, *ACS Nano* **9**, 5976 (2015).
- [26] S. Aftab, M. F. Khan, P. Gautam, H. Noh, and J. Eom, *Nanoscale* **11**, 9518 (2019).
- [27] Q. Li, S. Bi, K. Asare-Yeboah, J. Na, Y. Liu, C. Jiang, and J. Song, *ACS Nano* **13**, 8425 (2019).
- [28] S. Bi, Q. Li, K. Asare-Yeboah, J. Na, Y. Sun, and C. Jiang, *The Journal of Physical Chemistry Letters* **11**, 3947 (2020).
- [29] K. Asare-Yeboah, Q. Li, C. Jiang, Z. He, S. Bi, Y. Liu, and C. Liu, *The Journal of Physical Chemistry Letters* **11**, 6526 (2020).
- [30] H. Yoo, S. Hong, S. On, H. Ahn, H.-K. Lee, Y. K. Hong, S. Kim, and J.-J. Kim, *ACS Applied Materials & Interfaces* **10**, 23270 (2018).
- [31] Z. Yao, C. L. Kane, and C. Dekker, *Phys. Rev. Lett.* **84**, 2941 (2000).
- [32] D. K. Efetov and P. Kim, *Phys. Rev. Lett.* **105**, 256805 (2010).
- [33] B. Chakraborty, A. Bera, D. V. S. Muthu, S. Bhowmick, U. V. Waghmare, and A. K. Sood, *Phys. Rev. B* **85**, 161403 (2012).
- [34] B. Chakraborty, S. N. Gupta, A. Singh, M. Kuirri, C. Kumar, D. V. S. Muthu, A. Das, U. V. Waghmare, and A. K. Sood, *2D Materials* **3**, 015008 (2016).
- [35] H. Yuan, H. Shimotani, A. Tsukazaki, A. Ohtomo, M. Kawasaki, and Y. Iwasa, *Advanced Functional Materials* **19**, 1046 (2009).
- [36] C. Lu, Q. Fu, S. Huang, and J. Liu, *Nano Letters* **4**, 623 (2004).
- [37] M. A. Gebbie, H. A. Dobbs, M. Valtiner, and J. N. Israelachvili, *Proceedings of the National Academy of Sciences* **112**, 7432 (2015).
- [38] L. A. Jurado and R. M. Espinosa-Marzal, *Scientific Reports* **7**, 4225 (2017).
- [39] Y. Xia, W. Xie, P. P. Ruden, and C. D. Frisbie, *Phys. Rev. Lett.* **105**, 036802 (2010).
- [40] P. Gallagher, M. Lee, T. A. Petach, S. W. Stanwyck, J. R. Williams, K. Watanabe, T. Taniguchi, and D. Goldhaber-Gordon, *Nature communications* **6**, 1 (2015).
- [41] K. Ueno, S. Nakamura, H. Shimotani, A. Ohtomo, N. Kimura, T. Nojima, H. Aoki, Y. Iwasa, and M. Kawasaki, *Nature Materials* **7**, 855 (2008).
- [42] J. T. Ye, S. Inoue, K. Kobayashi, Y. Kasahara, H. T. Yuan, H. Shimotani, and Y. Iwasa, *Nature Materials* **9**, 125 (2010).
- [43] B. Karki, B. Freelon, M. Rajapakse, R. Musa, S. M. S. Riyadh, B. Morris, U. Abu, M. Yu, G. Sumanasekera, and J. B. Jasinski, *Nanotechnology* **31**, 425707 (2020).
- [44] M. Grzeszczyk, K. Gołasa, M. Zinkiewicz, K. Noga-jewski, M. R. Molas, M. Potemski, A. Wymolek, and A. Babiński, *2D Materials* **3**, 025010 (2016).
- [45] Q. Song, H. Wang, X. Pan, X. Xu, Y. Wang, Y. Li, F. Song, X. Wan, Y. Ye, and L. Dai, *Scientific Reports* **7**, 1758 (2017).
- [46] M. Kuirri, S. Das, D. V. S. Muthu, A. Das, and A. K. Sood, *Nanoscale* **12**, 8371 (2020).
- [47] A. Bera, A. Singh, D. V. S. Muthu, U. V. Waghmare, and A. K. Sood, *Journal of Physics: Condensed Matter* **29**, 105403 (2017).
- [48] X.-M. Zhao, H.-y. Liu, A. F. Goncharov, Z.-W. Zhao, V. V. Struzhkin, H.-K. Mao, A. G. Gavriliuk, and X.-J. Chen, *Phys. Rev. B* **99**, 024111 (2019).
- [49] A. Splendiani, L. Sun, Y. Zhang, T. Li, J. Kim, C.-Y. Chim, G. Galli, and F. Wang, *Nano Letters* **10**, 1271 (2010).
- [50] G. Stan, C. V. Ciobanu, S. R. J. Likith, A. Rani, S. Zhang, C. A. Hacker, S. Krylyuk, and A. V. Davydov, *ACS Applied Materials & Interfaces* **12**, 18182 (2020).
- [51] D. Qu, X. Liu, M. Huang, C. Lee, F. Ahmed, H. Kim, R. S. Ruoff, J. Hone, and W. J. Yoo, *Advanced Materials* **29**, 1606433 (2017).
- [52] J. Ribeiro-Soares, R. M. Almeida, E. B. Barros, P. T. Araujo, M. S. Dresselhaus, L. G. Cançado, and A. Jorio, *Phys. Rev. B* **90**, 115438 (2014).
- [53] M. Yamamoto, S. T. Wang, M. Ni, Y.-F. Lin, S.-L. Li, S. Aikawa, W.-B. Jian, K. Ueno, K. Wakabayashi, and K. Tsukagoshi, *ACS Nano* **8**, 3895 (2014).
- [54] R. Misra, M. McCarthy, and A. F. Hebard, *Applied Physics Letters* **90**, 052905 (2007).
- [55] Y.-F. Lin, Y. Xu, S.-T. Wang, S.-L. Li, M. Yamamoto, A. Aparecido-Ferreira, W. Li, H. Sun, S. Nakaharai, W.-B. Jian, K. Ueno, and K. Tsukagoshi, *Advanced Materials* **26**, 3263 (2014).
- [56] S. Fathipour, N. Ma, W. S. Hwang, V. Protasenko, S. Vishwanath, H. G. Xing, H. Xu, D. Jena, J. Appenzeller, and A. Seabaugh, *Applied Physics Letters* **105**, 192101 (2014).
- [57] P. Giannozzi, S. Baroni, N. Bonini, M. Calandra, R. Car, C. Cavazzoni, D. Ceresoli, G. L. Chiarotti, and M. C. *et al.*, *Journal of Physics: Condensed Matter* **21**, 395502 (2009).
- [58] X. Hua, X. Chen, and W. A. Goddard, *Phys. Rev. B* **55**, 16103 (1997).
- [59] J. P. Perdew, K. Burke, and M. Ernzerhof, *Phys. Rev. Lett.* **80**, 891 (1998).
- [60] A. D. Corso and A. M. Conte, *Phys. Rev. B* **71**, 115106 (2005).
- [61] S. Grimme, *Journal of Computational Chemistry* **25**, 1463 (2004).
- [62] T. Brumme, M. Calandra, and F. Mauri, *Phys. Rev. B* **89**, 245406 (2014).
- [63] S. Baroni, S. de Gironcoli, A. Dal Corso, and P. Giannozzi, *Rev. Mod. Phys.* **73**, 515 (2001).
- [64] O. Knop and R. D. MacDonald, *Canadian Journal of Chemistry* **39**, 897 (1961).

Supplemental Material

Symmetry induced phonon renormalization in few layers of 2H-MoTe₂ transistors: Raman and first-principles studies

Subhadip Das¹, Koyendrilla Debnath², Biswanath Chakraborty^{1,3}, Anjali Singh⁴,
Shivani Grover², D. V. S. Muthu¹, U. V. Waghmare² and A. K. Sood^{1*}

¹*Department of Physics, Indian Institute of Science, Bangalore 560012, India*

²*Theoretical Sciences Unit, Jawaharlal Nehru Centre for
Advanced Scientific Research, Bangalore-560064, India*

³*Present address: Department of Physics,
Indian Institute of Technology Jammu, Jammu-181221, J&K, India*

⁴*Center for Study of Science, Technology & Policy (CSTEP), Bangalore 560094, India.*

TABLE S1: Irreducible representation of the Raman modes at Γ -point for N-layer and bulk MoTe₂ [1]. The dagger symbols (\dagger) represent silent modes. The E_{1g} mode is absent in backscattering configuration [1]. The modes with E' symmetry are both Raman and infrared active [1].

Layer number	Zone-center phonon representation of the Raman modes					
	$\leq 30 \text{ cm}^{-1}$	$\leq 40 \text{ cm}^{-1}$	$\sim 120 \text{ cm}^{-1}$	$\sim 170 \text{ cm}^{-1}$	$\sim 235 \text{ cm}^{-1}$	$\sim 290 \text{ cm}^{-1}$
Odd Layer	$\frac{N-1}{2} E'$	$\frac{N-1}{2} A'_1$	$\frac{N-1}{2} E'$	$\frac{N+1}{2} A'_1$	$\frac{N+1}{2} E'$	$\frac{N-1}{2} A'_1$
Even layers	$\frac{N}{2} E_g$	$\frac{N}{2} A_{1g}$	$\frac{N}{2} E_g$	$\frac{N}{2} A_{1g}$	$\frac{N}{2} E_g$	$\frac{N}{2} A_{1g}$
Bulk	E_{2g}	B_{2g}^\dagger	E_{1g}	A_{1g}	E_{2g}	B_{2g}^\dagger

* asood@iisc.ac.in

I. Electrical and Raman spectral characterization of the bilayer MoTe₂ nanocrystal

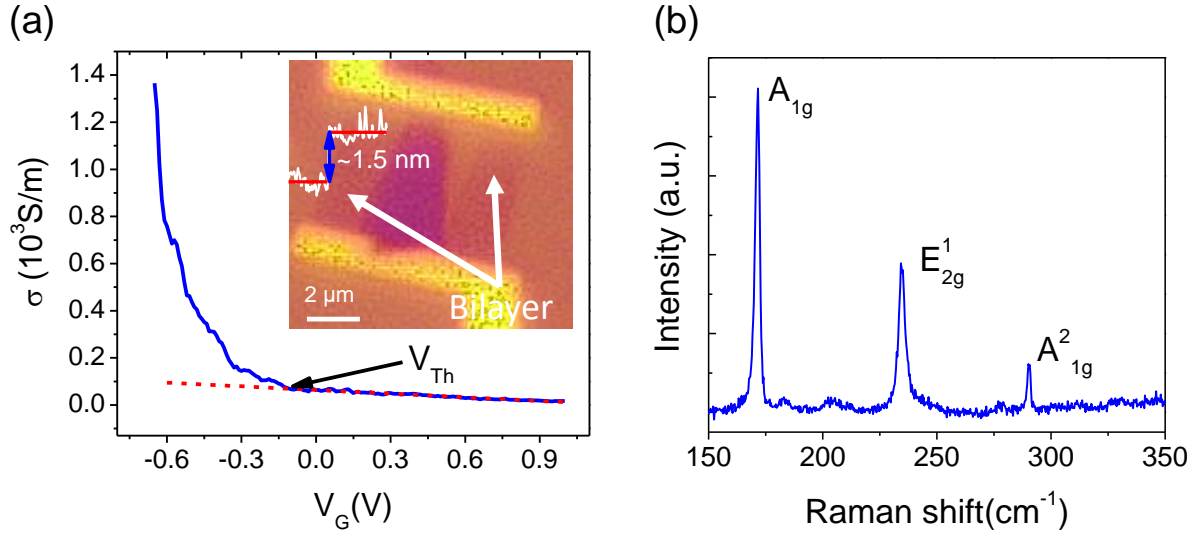


Fig. S1: (a) Transport characteristics of the field-effect device with bilayer and multilayer ($\sim 9\text{nm}$) parallel channel. The field effect mobility and current on/off ratio are $\sim 0.21 \text{ cm}^2/\text{V}\cdot\text{s}$ and 10^2 , respectively. The red dashed line indicates linear fit to the transistor off state. The current threshold voltage ($\sim -0.13\text{V}$) is indicated in the figure. Inset shows the AFM height profile with the optical image of the device. (b) Raman spectrum of the nanocrystal with 660 nm laser excitation.

II. Raman spectral background from the ionic liquid

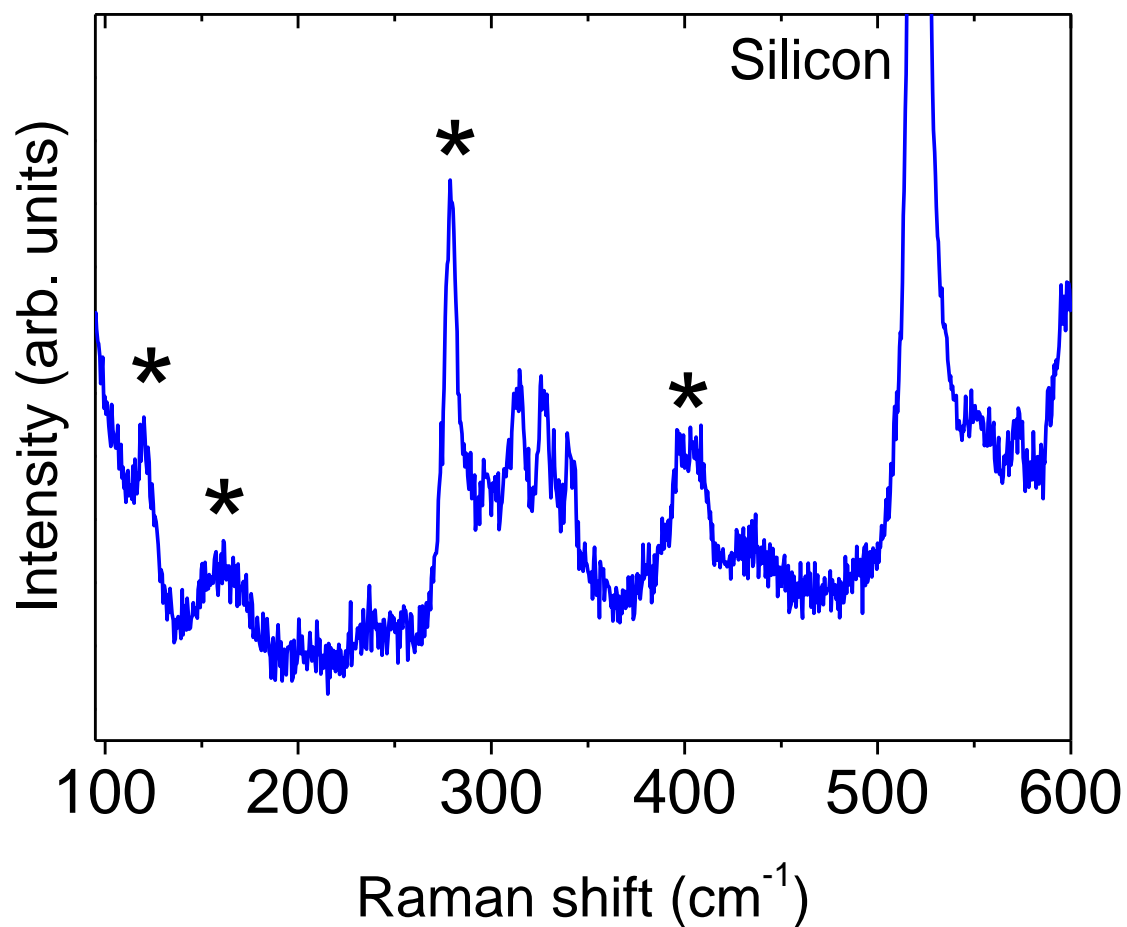


Fig. S2: Raman spectrum of EMIM-TFSI ionic liquid. The star symbol marks the Raman modes. The Raman mode at $\sim 520 \text{ cm}^{-1}$ is from the silicon substrate.

III. Output characteristics of the devices at ambient

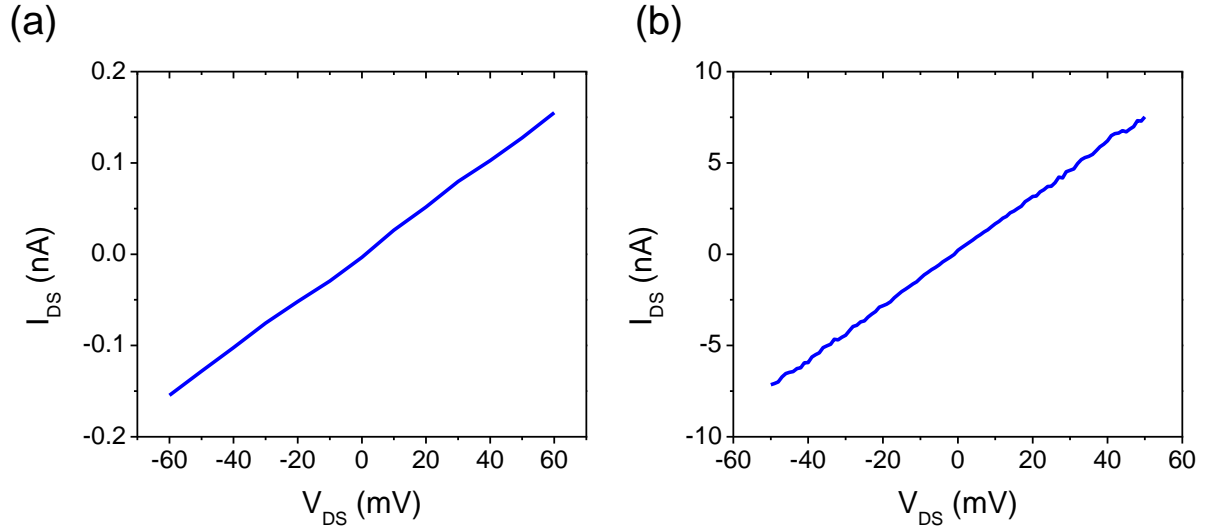


Fig. S3: Linear drain current (I_{DS}) versus drain voltage (V_{DS}) measurement at zero gate bias for (a) three- and (b) seven-layer nanocrystals.

-
- [1] G. Froehlicher, E. Lorchat, F. Fernique, C. Joshi, A. Molina-Sánchez, L. Wirtz, and S. Berciaud, Unified description of the optical phonon modes in n-layer mote2, Nano Letters **15**, 6481 (2015).